Journal of Advanced Ceramics
2022, **11**(6): 901–911
https://doi.org/10.1007/s40145-022-0584-4
ISSN 2226-4108
CN 10-1154/TQ

Research Article

Optical, thermal, and mechanical properties of $(Y_{1-x}Sc_x)_2O_3$ transparent ceramics

Changliang YANG[a,b], Jiquan HUANG[a,b,c,*], Qiufeng HUANG[b], Zhonghua DENG[b,c], Yun WANG[a,b], Xiaoyun LI[a,b], Zehua ZHOU[a,b], Jian CHEN[b,c], Zhuguang LIU[b,c], Wang GUO[b,c,*]

[a]*College of Chemistry and Materials Science, Fujian Normal University, Fuzhou 350117, China*
[b]*Key Laboratory of Optoelectronic Materials Chemistry and Physics, Fujian Institute of Research on the Structure of Matter, Chinese Academy of Sciences, Fuzhou 350002, China*
[c]*Fujian Science & Technology Innovation Laboratory for Optoelectronic Information of China, Fuzhou 350108, China*

Received: November 25, 2021; Revised: February 23, 2022; Accepted: February 27, 2022

Abstract: Sesquioxides such as Y_2O_3 and Sc_2O_3 are important optical materials, but the fabrication of their transparent ceramics remains a challenge due to the ultra-high melting point of over 2400 ℃. In this work, a series of $(Y_{1-x}Sc_x)_2O_3$ transparent ceramics were successfully fabricated by a simple vacuum sintering process without any sintering additives, and the effect of scandium (Sc) content (x) on the crystal structure and optical/thermal/mechanical properties was evaluated. Y_2O_3 and Sc_2O_3 form a complete solid solution with a cubic bixbyite structure. The formation of $(Y_{1-x}Sc_x)_2O_3$ solid solution promotes the densification of ceramics, leading to the realization of high transparency close to the theoretical transmittance over a wide wavelength range of 0.35–8 μm. In particular, the in-line transmittance in the range of 0.6–6 μm remains above 80% for $(Y_{1-x}Sc_x)_2O_3$ with x = 0.23–0.31, while the pristine Y_2O_3 and Sc_2O_3 are opaque. Moreover, the mechanical properties including Vickers hardness (HV), fracture toughness (K_{IC}), and biaxial flexural strength (δ_b) are evidently enhanced due to the solid solution strengthening, while the thermal conductivity (k) is reduced due to the reduction of photon free path. This study demonstrates that forming of solid solution is a facile and universal approach for preparing sesquioxide transparent ceramics with high optical and mechanical quality.

Keywords: Y_2O_3; Sc_2O_3; solid solution transparent ceramics; thermal conductivity; mechanical properties

1 Introduction

Y_2O_3, Sc_2O_3, and Lu_2O_3 are bixbyite-type sesquioxide crystals with the same cubic structure, and the space group is $Ia\bar{3}$ (206) [1]. These sesquioxides have similar physical and chemical properties, such as strong corrosion resistance, high thermal stability, high thermal conductivity (k) (12–18 W/(m·K)), wide band-gap (5.6–6.0 eV), wide range of optical transparency wavelength (0.3–8 μm), low maximum phonon energy, and high refractive index (1.88–1.97) [1–8]. Owing to

* Corresponding authors.
E-mail: J. Huang, hjq@fjirsm.ac.cn;
W. Guo, guowang@fjirsm.ac.cn

these superior characteristics, Y_2O_3, Sc_2O_3, and Lu_2O_3 are excellent scintillators and laser hosts, in particular, they are more suitable for high-performance and ultrafast laser applications compared with $Y_3Al_5O_{12}$ (YAG) [1,9–11]. Also, they are considered as promising candidates for the next generation of infrared (IR) windows operating in harsh environments [12]. However, their extremely high melting point (> 2400 ℃) complicates the growth of single crystals and the fabrication of transparent ceramics with high quality and large size. Lowering down the synthesis temperature has thus become the most important solution. In this regard, an effective strategy, parallel to the improvement of sintering technology and powder engineering, is to introduce sintering additives. In the past decades, various sintering additives, such as LiF [13], CaO [14], ZrO_2 [15], HfO_2 [16], TiO_2 [17], and La_2O_3 [18], have been adopted to promote the densification of sesquioxide transparent ceramics at a sintering temperature far below the melting point, and it is found that the in-line transmittance and even the laser performances of the resultant ceramics can be comparable to those of single crystals [1]. However, the utilization of sintering additives also introduces secondary phases, which aggravates the scattering and decreases the quality of the transparent ceramics [19].

Recently, an alternative method of synthesizing sesquioxide transparent ceramics (and single crystals) has been proposed, which is to reduce the synthesis temperature by forming a solid solution [1,20]. It is found that Y_2O_3, Sc_2O_3, and Lu_2O_3 can be mixed in arbitrary ratios to form complete solid solution series with the formula of $(Lu_xY_ySc_{1-x-y})_2O_3$ ($0 \leqslant x < 1$, $0 \leqslant y < 1$, and $0 < x + y \leqslant 1$), and the melting (or liquidus) points of the binary and ternary systems are generally lower than those of any constituent component [1,20–25]. For example, the melting points of Y_2O_3, Sc_2O_3, and Lu_2O_3 are around 2450 ℃, while those of their solid solution $(Y_{0.55}Sc_{0.45})_2O_3$, $(Lu_{0.55}Sc_{0.45})_2O_3$, $(Lu_{0.55}Y_{0.45})_2O_3$, and $(Lu_{0.2}Y_{0.4}Sc_{0.4})_2O_3$ are about 2050, 2350, 2340, and 2110 ℃, respectively [1,26,27]. It is worth noting that the melting points of Y_2O_3 and Sc_2O_3 can be reduced by up to ~400 ℃ by forming a solid solution, which facilitates the synthesis of high-purity, high-quality transparent ceramics. Furthermore, Y_2O_3 is one of the most excellent hosts for mid-IR laser operation due to its lowest maximum phonon energy (~591 cm^{-1}), while Sc_2O_3 possesses higher thermal capacity, thermal conductivity (k), and Young's modulus than Y_2O_3 [21]. The synergy of these advantages may occur in the $(Y_{1-x}Sc_x)_2O_3$ solid solution. In fact, several studies have shown that for the solid solutions, not only ultrashort pulse laser and larger emission bandwidths than those of constituent sesquioxide can be achieved, but also the mechanical toughness and hardness can be enhanced [26–28]. Therefore, excellent optical and mechanical properties are highly anticipated in the pristine and rare-earth-doped Sc_2O_3–Y_2O_3 solid solution.

In this work, with cheap commercial Y_2O_3 and Sc_2O_3 micron powders as starting materials, we fabricated a series of $(Y_{1-x}Sc_x)_2O_3$ transparent ceramics by the simple vacuum sintering method, and investigated the influence of scandium (Sc) content (x) on the crystal structure, densification, optical transmittance, and thermal and mechanical properties of the ceramics.

2 Experimental

2.1 Fabrication of $(Y_{1-x}Sc_x)_2O_3$ ceramics

High purity Y_2O_3 and Sc_2O_3 (99.99%) powders (with average particle sizes of ~2.5 and ~13 μm, respectively, as shown in Fig. S1 in the Electronic Supplementary Material (ESM)) were used as starting materials. The oxide powders were mixed according to the chemical formula of $(Y_{1-x}Sc_x)_2O_3$ ($0 \leqslant x < 0.5$), and ball-milled in absolute ethanol for 22 h. The as-obtained slurry was dried, ground, and sieved through a 100-mesh sieve. The powders were uniaxially compressed at 8 MPa to form a green body, and then cold isostatically pressed at 200 MPa for 1 min. Subsequently, the $(Y_{1-x}Sc_x)_2O_3$ green bodies were vacuum sintered at 1800 ℃ for 20 h, followed by annealing at 1200 ℃ for 10 h in the air. The as-obtained ceramics were mirror-polished to facilitate subsequent characterization.

2.2 Characterization

The phase compositions of the ceramics were examined by the powder X-ray diffractometer (Mini Flex600, Rigaku, Japan) using Cu Kα radiation. The theoretical density of the ceramics was calculated based on the X-ray diffraction (XRD) patterns, while the experimental bulk density was determined by the Archimedes method using absolute ethyl alcohol at room temperature. The morphology was observed by the scanning electron microscope (SEM; SU-8010, Hitachi, Japan), and the energy dispersive X-ray (EDX) spectroscope was used to identify the chemical compositions. The optical

transmittance (and reflection) was measured by an ultraviolet–visible–near-infrared (UV–Vis–NIR) spectrophotometer (Lambda950, PerkinElmer company, USA) in the wavelength range of 0.2–2.5 μm, and IR transmittance was measured by the FT-IR spectrometer (VERTEX 70, Bruker, Germany) ranging from 2.5 to 10 μm.

For the thermal-expansion measurement, the samples were cut into 4 mm × 3 mm × 25 mm and measured on the dilatometry DIL 402PC (NETZSCH, Germany). Thermal diffusion coefficient and specific heat of the transparent ceramics were measured by the laser flash method using a laser flash apparatus (LFA457, Nanoflash, Netzsch, Germany). For the sample with isotropic cubic structure, the linear thermal expansion coefficient (α) can be calculated by Eq. (1) [29]:

$$\alpha = \frac{1}{L_0}\frac{\mathrm{d}L}{\mathrm{d}T} \tag{1}$$

where L_0 is the initial length of the specimen and dL is the change in length within the temperature interval (dT). The thermal conductivity (k) as a function of temperature can be calculated using Eq. (2) [30]:

$$k(T) = \lambda(T) \cdot \rho(T) \cdot c_p(T) \tag{2}$$

where $\lambda(T)$, $\rho(T)$, and $c_p(T)$ are the thermal diffusivity, density, and heat capacity at temperature T, respectively.

The Vickers hardness (HV) and fracture toughness (K_{IC}) of the $(Y_{1-x}Sc_x)_2O_3$ transparent ceramics (ϕ20 mm × 1 mm) were obtained from 20 indentations made by the Digital Vickers Hardness Tester HV-1000IS (Shanghai Jujing Instrument Co., Ltd., China). The biaxial flexural strength (δ_b) was measured by the three-point bending method using the machined ceramic bars (3 mm × 4 mm × 36 mm; five bars were measured for each sample) on a universal tester (Instron 1195, Instron, USA). HV and K_{IC} are estimated by Eqs. (3) and (4) [31]:

$$HV = S\frac{P}{d^2} \tag{3}$$

$$K_{IC} = 0.018\left(\frac{E}{HV}\right)^{1/2}\left(\frac{P}{l^{3/2}}\right) \tag{4}$$

where d is the length of the indentation diagonal; P is the load on the indenter, which is equal to 9.8 N; S is the shape factor of the indenter, which is equal to 1.854 for a pyramid-shaped indentation; E is the Young's modulus, which is considered to be 179.8 GPa for Y_2O_3 [32]; $l = c - a$ (a is the length of the half-diagonal of the indent and c is the half-length of the indentation crack).

3 Results and discussion

The XRD patterns of the $(Y_{1-x}Sc_x)_2O_3$ ceramics, as well as the standard diffraction profiles of Y_2O_3 (JCPDS Card No. 41-1105) and Sc_2O_3 (JCPDS Card No. 42-1463), are presented in Fig. 1 and Fig. S2 in the ESM. For the pristine Y_2O_3 ceramic, all the diffraction peaks matched well with the standard PDF#41-1105 (Fig. S2 in the ESM) and thus could be indexed in terms of the cubic bixbyite structure with the space group $Ia\bar{3}$ (206). The incorporation of Sc_2O_3 into Y_2O_3 matrix resulted

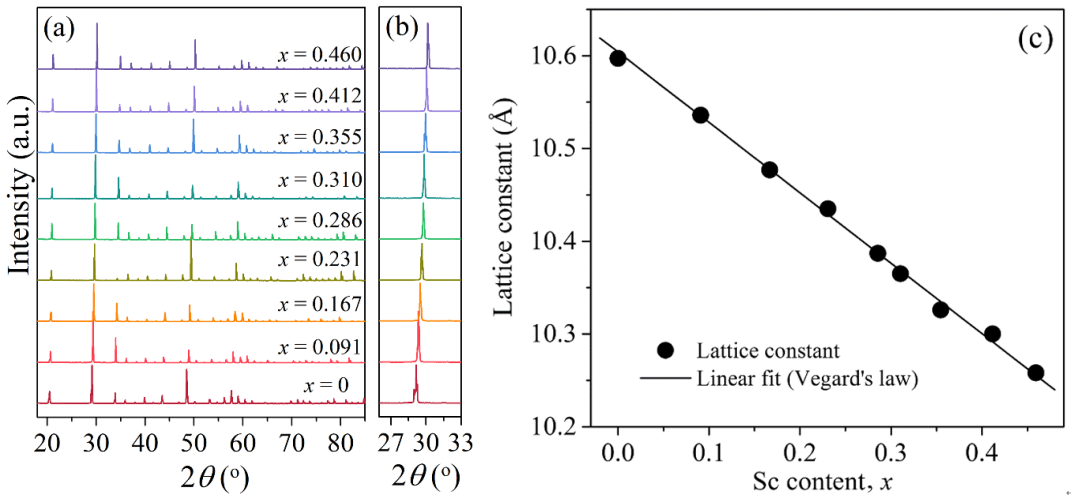

Fig. 1 (a) XRD patterns of the $(Y_{1-x}Sc_x)_2O_3$ ceramics. (b) Enlarged patterns from 26.6° to 36.0°. (c) Dependence of the lattice constant on the Sc content, x. The solid line represents the fitting result calculated using the Vegard's law with an expression of $a(x) = xa_{Sc} + (1 - x)a_Y$.

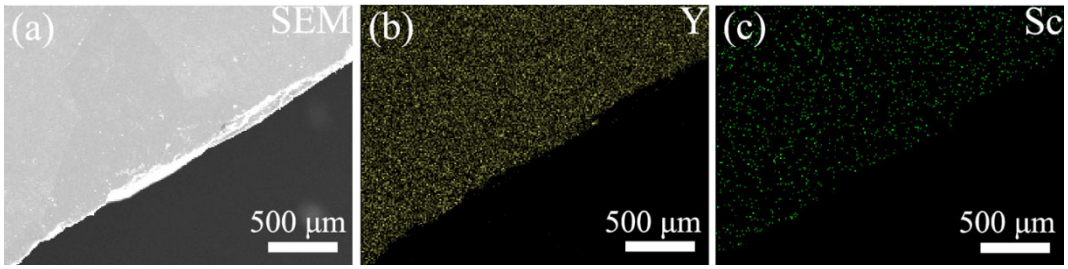

Fig. 2 (a) SEM image of $(Y_{0.769}Sc_{0.231})_2O_3$ transparent ceramic surface and the corresponding EDS mappings of (b) Y and (c) Sc elements.

in the shift of the diffraction peaks to a higher 2θ angle without the appearance of additional peaks (Fig. 1(a)), indicating the formation of Sc_2O_3–Y_2O_3 complete solid solution series. It was reported that perovskite-type $YScO_3$ (rare earth scandate) could be obtained by calcining the raw materials (Sc_2O_3–Y_2O_3 mixture) in the air at 1400 ℃ [33,34]. $YScO_3$ has orthogonal symmetry and has a birefringence effect at the grain boundary, which is harmful to the transparency of ceramics. Therefore, the partial formation of the perovskite phase should be avoided. As shown in Fig. 1(a), diffraction peaks attributed to the perovskite structure did not appear in the XRD patterns of the $(Y_{1-x}Sc_x)_2O_3$ ceramics. The reason can be explained as follows. In the Ln_2O_3–Sc_2O_3 (Ln stands for the rare earth elements Y, La, Nd, Sm, Yb, Lu, etc.) system, as the radius of the Ln^{3+} ion decreases, the formation of the perovskite phase becomes increasingly difficult [35–37]. For example, perovskite compounds ($LnScO_3$) can be synthesized for larger Ln ions ranging from La to Tb, while for Ln = Er, Tm, Yb, and Lu, only cubic solid solutions are formed. The ionic radius of Y^{3+} (as well as Dy^{3+} and Ho^{3+}) is between Tb^{3+} and Er^{3+}; therefore, the formation of $YScO_3$ (as well as $DyScO_3$ and $HoScO_3$) requires harsh conditions such as high pressures. The theoretical densities of perovskite-type $YScO_3$ and bixbyite-type $(Y_{0.5}Sc_{0.5})_2O_3$ solid solution are calculated to be 4.95 and 4.53 g/cm^3, respectively, which means that the perovskite phase is preferred at higher pressures. Clark *et al.* [35] reported that cubic solid solution with trace of perovskite was formed after calcining the Y_2O_3–Sc_2O_3 mixture at ambient pressure (~0.1 MPa) while single-phase $YScO_3$ was yielded at a higher pressure of 20,000 MPa. In this work, $(Y_{1-x}Sc_x)_2O_3$ ceramics were vacuum sintered. The low pressure (~1×10^{-3} Pa) blocks the formation of the perovskite phase and ensures the realization of a complete solid solution. Interestingly, we further treated these $(Y_{1-x}Sc_x)_2O_3$ ceramics at 180 MPa, 1700 ℃ for 3 h, and found that they remained cubic solid solution without forming a perovskite phase (Fig. S3 in the ESM), which highlights the thermodynamic stability of the cubic bixbyite structure.

For all the samples, the (222) peaks (located at 2θ = 29°–30.5°, in Fig. 1(b)) were intensive and sharp, and the full width at half maximum (FWHM) was almost the same, indicating that the Sc element was uniformly distributed in the Y_2O_3 matrix, which was further demonstrated by the energy dispersive spectroscopy (EDS) observation. Figure 2 shows the EDS elemental mappings of the $(Y_{0.769}Sc_{0.231})_2O_3$ ceramic, and Fig. S4 in the ESM shows the energy dispersive X-ray analysis (EDAX) line scans of the $(Y_{0.714}Sc_{0.286})_2O_3$ ceramic. Both Y and Sc elements were homogeneous distributed, which highlighted the formation of $(Y_{1-x}Sc_x)_2O_3$ solid solution without local aggregation or second phases. As aforementioned, the diffraction peaks of $(Y_{1-x}Sc_x)_2O_3$ shifted to a higher 2θ angle with increasing Sc content (Fig. 1(b)), which was attributed to the decrease in the lattice constant. The effective ionic radius is 0.745 Å for Sc^{3+} and 0.90 Å for Y^{3+} in 6-coordinate environments. Therefore, the substitution of Y^{3+} ions by smaller Sc^{3+} ions must result in the shrinkage of the unit cell. According to the XRD patterns, the lattice constant of $(Y_{1-x}Sc_x)_2O_3$ was calculated and presented in Fig. 1(c). The lattice constant has a linear relationship with Sc content (x), and agrees well with the theoretical value calculated by Vegard's law, that is, $a(x) = xa_{Sc} + (1 - x)a_Y$, where $a(x)$, a_{Sc} = 9.845 Å, and a_Y = 10.604 Å are the lattice constants of $(Y_{1-x}Sc_x)_2O_3$, Sc_2O_3, and Y_2O_3, respectively. We can thus conclude that Y and Sc elements are randomly distributed in the cation sites of the cubic lattice, and the lattice constant of the solid solutions follows the rule of mixture.

Figure 3 presents the cross-sectional morphologies of the $(Y_{1-x}Sc_x)_2O_3$ ceramics. It is readily apparent that the microstructures of the samples are closely related to the content of Sc_2O_3. As shown in Fig. 3(a), considerable residual pores existed in the pristine Y_2O_3 ceramics. The ceramics became more densified with the introduction

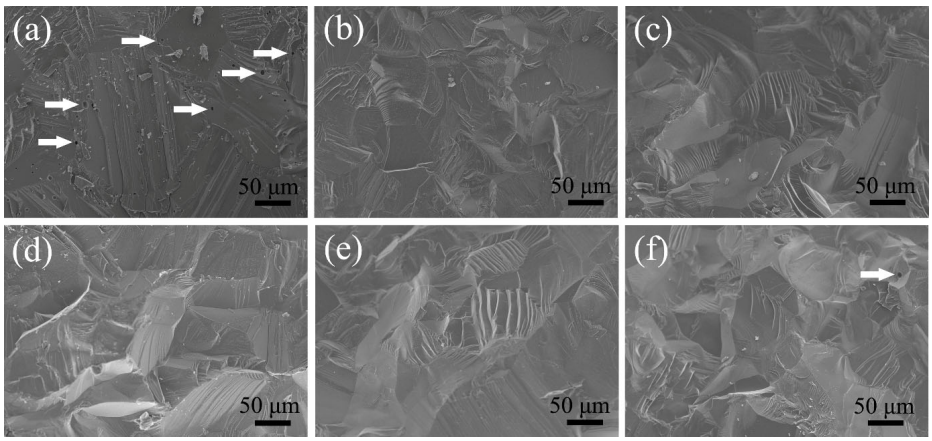

Fig. 3 Cross-sectional SEM images of $(Y_{1-x}Sc_x)_2O_3$ ceramics with (a) $x = 0$, (b) $x = 0.091$, (c) $x = 0.184$, (d) $x = 0.286$, (e) $x = 0.355$, and (f) $x = 0.412$.

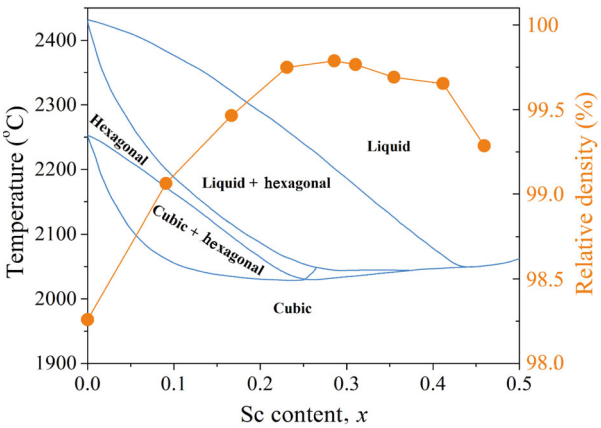

Fig. 4 Relative densities of the $(Y_{1-x}Sc_x)_2O_3$ transparent ceramics and phase diagram of binary Y_2O_3–Sc_2O_3 system [7,24].

of Sc. Large pores were not observed in the SEM images of $(Y_{1-x}Sc_x)_2O_3$ ceramics with $x = 0.184$–0.355 (Figs. 3(c)–3(e)). As the Sc_2O_3 content further increased to 0.412, few pores appeared again (Fig. 3(f)). Obviously, the densification of Y_2O_3 ceramics can be effectively improved by incorporating an appropriate amount of Sc_2O_3, which is beneficial to the fabrication of transparent ceramics. Figure 4 shows the variation of the relative density of the $(Y_{1-x}Sc_x)_2O_3$ ceramics with Sc content (x). The relative densities increased remarkably with Sc content (x) and reached the highest value of 99.79% when $x = 0.286$, above which the relative densities turned to decrease. The pronounced dependence of the porosity on composition is believed to be related to the change in melting point. To confirm this viewpoint, Fig. 4 also presents the binary phase diagram of the Y_2O_3–Sc_2O_3 system with Sc_2O_3 content of 0%–50% ($0 \leqslant x \leqslant 0.5$). It is found that the melting temperature drops sharply from 2430 ℃ of Y_2O_3 to below 2100 ℃ of $(Y_{1-x}Sc_x)_2O_3$ with $x > 0.18$, which is essential for improving the densification of the ceramics.

Figure 5(a) shows the photographs of the $(Y_{1-x}Sc_x)_2O_3$ ceramics with the same thickness of 1 mm, while Figs. 5(b) and 5(c) display their UV–Vis–NIR (200–2500 nm) and IR (2500–11,000 nm) transmittance spectra, respectively. It is found that the optical transmittance of Y_2O_3 can be enhanced markedly by Sc incorporation. The pristine Y_2O_3 ceramic was opaque (the in-line transmittance was lower than 1% within the visible region). However, for the $(Y_{1-x}Sc_x)_2O_3$ samples, with increasing Sc content (x), the transparence of the ceramics increased greatly and reached the maximum at $x \approx 0.286$, and then turned to decrease gradually, which was consistent with the observation of morphology and density (Figs. 3 and 4). With 16%–36% Sc_2O_3 incorporation, the samples were highly transparent over a wide wavelength range of 350–8000 nm. For example, the in-line transmittance at 4000 nm was as high as 81.5%, 82.2%, 80.2%, 81.8%, and 79.6% for $(Y_{1-x}Sc_x)_2O_3$ samples with $x = 0.167$, 0.231, 0.259, 0.286, and 0.310, respectively. Similarly, the transmittance of the sample $(Y_{0.714}Sc_{0.286})_2O_3$ ($x = 0.286$) was 81.3%@600 nm, 82.3%@2000 nm, 81.8%@4000 nm, and 81.7%@6000 nm (Fig. 5(d)), which were close to the theoretical values of Y_2O_3 single crystal (81.9%@600 nm and 82.4%@2000 nm). The high transparency and the broad transparency range highlight the excellent quality of the $(Y_{1-x}Sc_x)_2O_3$ transparent ceramics.

The transmittance of the $(Y_{1-x}Sc_x)_2O_3$ transparent ceramics exhibited a sharp decline in both the IR and UV regions. The IR cutoff was controlled by multi-phonon interactions, while the UV edge was attributed to the absorption across the band gap (i.e., the electronic transition from the valence band to conduction band)

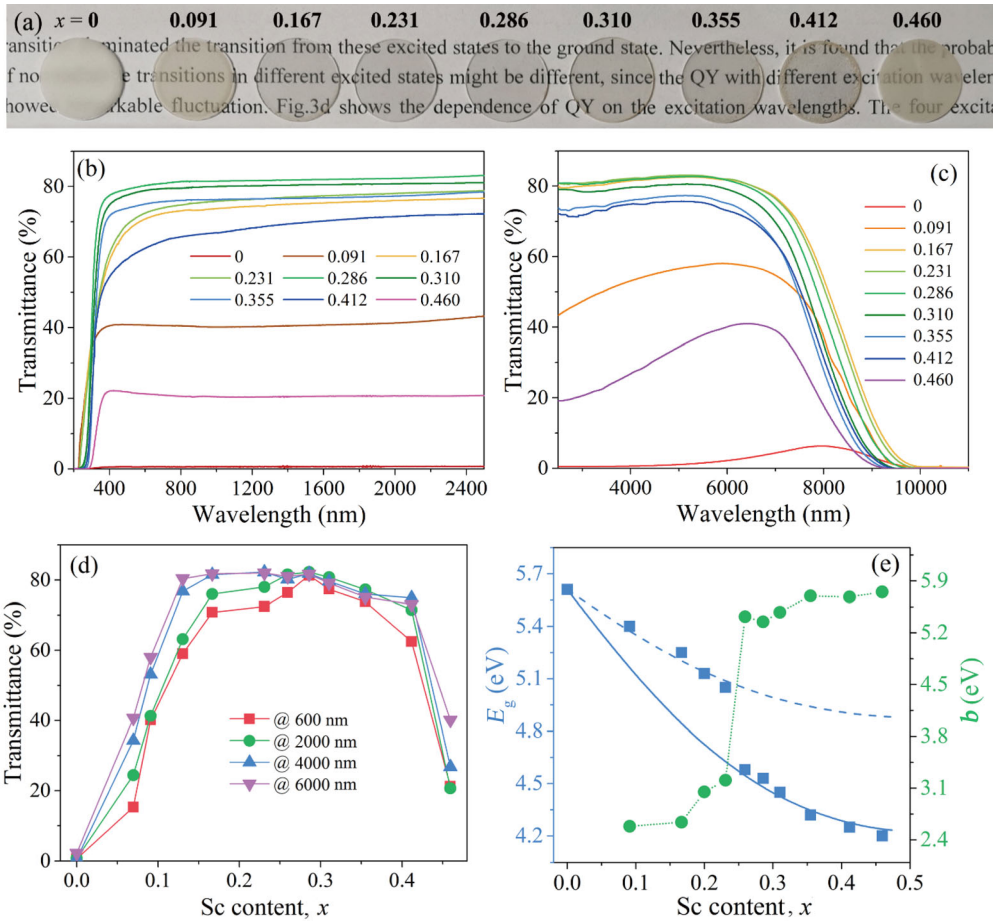

Fig. 5 (a) Photographs and in-line (b) UV–Vis–NIR and (c) IR transmission spectra of the $(Y_{1-x}Sc_x)_2O_3$ ceramics. (d) Dependence of the transmittance at different wavelength on Sc content (x). (e) Optical band-gap (E_g) and bowing coefficient (b) as plots of Sc content (x). The solid and dash blue lines represent the fitting result with the expression of $E_g(x) = xE_g(Sc_2O_3) + (1-x)E_g(Y_2O_3) - bx(1-x)$ by setting b = 5.6 and 3.0, respectively. The green dot line is only to guide the eye.

[37–39]. The optical band-gap (E_g) of the $(Y_{1-x}Sc_x)_2O_3$ ceramics was calculated from the UV cutoff curves by using the Tauc formula [40], and the results are presented in Fig. 5(e). The value of E_g was 5.61 eV for Y_2O_3 and 5.65 eV for Sc_2O_3 (Fig. S5 in the ESM). For the $(Y_{1-x}Sc_x)_2O_3$ ceramics, the band-gap decreased significantly with increasing Sc content (x). Especially, the value of E_g fell into the range of 4.2–4.6 eV when $x > 0.25$, which was far smaller than that of Y_2O_3 and Sc_2O_3. The deviation of the experimental values from Vegard's law can be attributed to the band-gap bowing effect [41,42]. For isovalent semiconductor (or insulator) compounds $A_xB_{1-x}C$, because of the atomic size and orbital energy differences between A and B, the local crystal symmetry is distorted, and isovalent defect levels may also be induced [43,44]. As a result, the band-gap is narrowed, which is manifested as the downward bowing of the curve of band-gap $E_g(x)$ vs. Sc content. Such band-gap bowing can be described by a quadratic equation: $E_g(x) = xE_g(AC) + (1-x)E_g(BC) - bx(1-x)$, where b is the bowing parameter, and $E_g(AC)$ and $E_g(BC)$ are the band-gaps of the constituents AC and BC, respectively [44,45]. As shown in Fig. 5(e), with increasing Sc content (x), b increased slightly when $x < 0.23$ and when $x > 0.26$, but increased sharply (from ~3.0 to ~5.4 eV) when $x \approx 0.25$. This phenomenon is analogous to the percolation effect. The percolation effect can be simply understood as an abrupt change of a certain physical property (such as dielectric constant, elastic modulus, electrical conductivity, and thermal conductivity (k)) near the percolation threshold. The percolation threshold (x_p) is a mathematical concept that describes the formation of long-range connectivity in random networks, which is defined as the critical value of the occupation probability (or the minimum fraction of the occupied sites) forming an infinite connected cluster [46,47]. For example, an infinite chain of Sc–O–Sc–O bonds forms in the $(Y_{1-x}Sc_x)_2O_3$ solid

solution when $x \geqslant x_p$, while only isolated Sc–O bonds or finite Sc–O–Sc–O chains exist when $x < x_p$. As shown in Fig. 5(e), the b value has a sudden change near $x = 0.25$ for $(Y_{1-x}Sc_x)_2O_3$, which is consistent with the theoretical value of $x_p = 0.245$ for body-centered cubic Bravais lattice. However, at present, there is not enough evidence to prove that the band-gap bowing is related to the percolation effect.

In addition to the optical properties, thermal and mechanical performances are also important indicators for transparent ceramics. Figure 6(a) shows the dependence of thermal expansion (dL/L_0) on temperature. Since the dilatometer furnace was not stable around room temperature and at the initial stage, the thermal expansion coefficients (α) were not accurate below 500 K. At temperatures above 500 K, the thermal expansion (dL/L_0) curves were essentially linear, and were almost independent of composition. For example, the values of dL/L_0 at 900 K were 0.00427, 0.00446, 0.00458, 0.00448, and 0.00447 for $(Y_{1-x}Sc_x)_2O_3$ with x = 0, 0.167, 0.286, 0.355, and 0.460, respectively. Figure 6(b) plots the thermal expansion coefficient (α) vs. temperature for the $(Y_{1-x}Sc_x)_2O_3$ samples. It was found that the incorporation of Sc resulted in a slight increase in the thermal expansion coefficient (α), which can be attributed to the higher thermal expansion coefficient (α) of Sc_2O_3 relative to Y_2O_3 [21].

Figure 7(a) shows the variations of the heat capacity (c_p) and thermal diffusivity (λ) of the $(Y_{1-x}Sc_x)_2O_3$ transparent ceramics with Sc content (x). The thermal diffusivity (λ) decreased monotonically with increasing Sc content (x), from 3.66 mm^2/s for pristine Y_2O_3 ($x = 0$) to 1.48 mm^2/s for $(Y_{0.645}Sc_{0.355})_2O_3$ (x = 0.355). In contrast, since the heat capacity (C_p) of Sc_2O_3 is higher than that of Y_2O_3 [17], the addition of Sc increases the

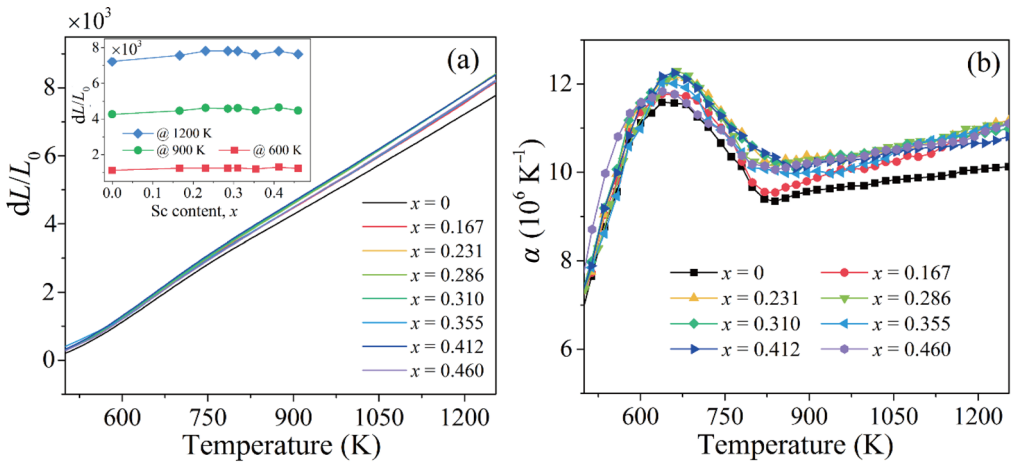

Fig. 6 (a) Thermal expansion (dL/L_0) and (b) thermal expansion coefficient (α) of the $(Y_{1-x}Sc_x)_2O_3$ transparent ceramics as a function of temperature. The inset in (a) shows the dependence of the thermal expansion (dL/L_0) on Sc content (x) under different temperatures.

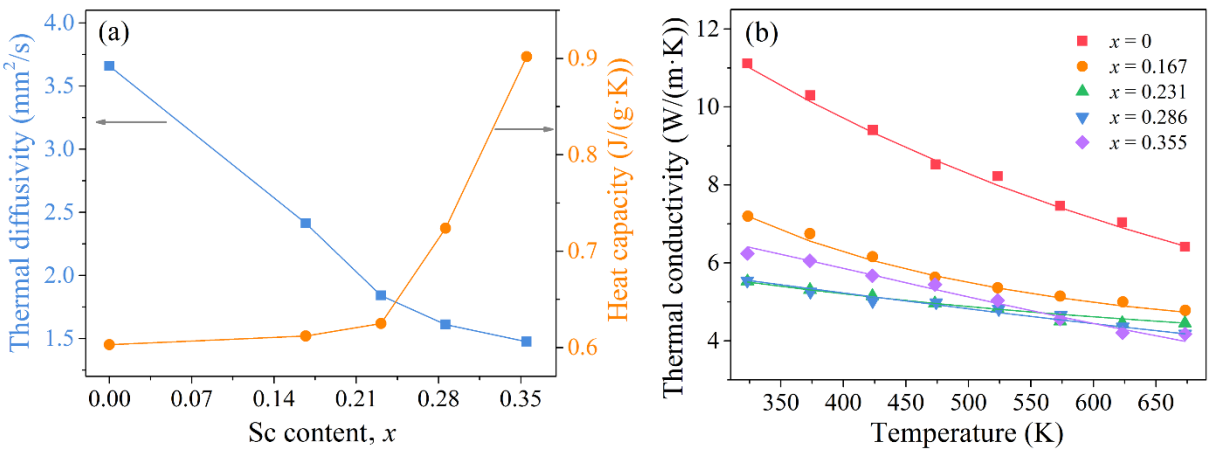

Fig. 7 (a) Dependence of the room-temperature thermal diffusivity (λ) and heat capacity (c_p) of the $(Y_{1-x}Sc_x)_2O_3$ transparent ceramics on Sc content (x); (b) thermal conductivity (k) of the $(Y_{1-x}Sc_x)_2O_3$ transparent ceramics as a function of temperature. The solid lines represent the fitting results calculated using Eq. (5).

heat capacity (c_p) of the sample. According to the empirical Neumann–Kopp rule [33], the heat capacity (c_p) of the $(Y_{1-x}Sc_x)_2O_3$ solid-state solution is approximately equal to the stoichiometric sum of the respective capacities of Sc_2O_3 and Y_2O_3.

Based on the experimental-determined thermal diffusivity (λ), heat capacity (c_p), and density, the thermal conductivities (k) of the $(Y_{1-x}Sc_x)_2O_3$ ceramics were calculated by Eq. (2) and displayed in Fig. 7(b). The thermal conductivity (k) decreased with increasing temperature, which can be well described by Eq. (5) [5,42]:

$$k(T) = \frac{1}{a + bT + cT^2} \tag{5}$$

where a, b, and c are constants, which therefore implies that the thermal conductivity (k) is dominated by four-phonon heat transport [30]. The phonon mean free path is reduced by the phonon scattering and goes as $1/T$ above the Debye temperature, which causes the thermal conductivity (k) to decrease at higher temperatures [42]. Meanwhile, due to the mismatch of the atomic mass and ionic radii between Y^{3+} and Sc^{3+}, the incorporation of Sc into the Y_2O_3 matrix will cause structural deformation, which also reduces the phonon mean free path. As a result, the room-temperature thermal conductivity (k) was decreased from 11.12 W/(m·K) for pristine Y_2O_3 (x = 0) to 7.20, 5.53, 5.55, and 6.24 W/(m·K) for $(Y_{1-x}Sc_x)_2O_3$ with x = 0.167, 0.231, 0.286, and 0.355, respectively, as shown in Fig. 7(b). According to Eq. (2), the thermal conductivity (k) is determined by the thermal diffusivity (λ), density (ρ), and heat capacity (c_p). As aforementioned, with increasing Sc content (x), both the thermal diffusivity (λ) and density (ρ) decrease, which reduces the thermal conductivity (k). However, the heat capacity (c_p) increases, which improves the thermal conductivity (k). Consequently, the overall decrease in thermal conductivity (k) is limited greatly. It is noted that the thermal conductivity (k) of the $(Y_{1-x}Sc_x)_2O_3$ transparent ceramics is comparable with that of Y_2O_3 ceramics doped with rare earth (such as 0.5%Nd:Y_2O_3) [41] and with sintering aid (such as 2.72 wt% ZrO_2 doped Y_2O_3) [15], and is higher than that of traditional laser glass.

Good mechanical properties and damage tolerance are of great significance to the reliability and machinability of ceramics. Several key mechanical performance indicators, including the Vickers hardness (HV), fracture toughness (K_{IC}), and biaxial flexural strength (δ_b), are summarized in Table 1. It is found that $(Y_{1-x}Sc_x)_2O_3$ solid solutions have more excellent mechanical performances than those of the constituent oxides. For example, the Vickers hardness (HV) of $(Y_{1-x}Sc_x)_2O_3$ with x = 0.231, 0.286, and 0.310 was ~9.44, ~9.69, and ~9.62 GPa, respectively, which was much higher than that of Y_2O_3 (6.71 GPa) and Sc_2O_3 (6.75 GPa). The fracture toughness (K_{IC}) increased from 1.16 MPa·m$^{1/2}$ for pristine Y_2O_3 (and 1.21 MPa·m$^{1/2}$ for Sc_2O_3) to 1.56 MPa·m$^{1/2}$ for the sample with x = 0.231 (and 1.40 MPa·m$^{1/2}$ for x = 0.286). Similarly, the biaxial flexural strength (δ_b) of $(Y_{1-x}Sc_x)_2O_3$ with x = 0.231, 0.286, and 0.310 were 31%, 37%, and 48% higher than that of Y_2O_3, respectively. Since the average grain sizes of the ceramics was larger than 50 μm (Fig. S6 in the ESM), the mechanical properties depend slightly on the grain size. Therefore, the improved mechanical properties can be mainly attributed to the solid solution strengthening originating from lattice distortion [48,49]. Ideally, all atoms of a crystalline material locate perfectly in their lattice sites. However, for a solid solution such as $(Y_{1-x}Sc_x)_2O_3$, larger Y atoms push away their neighbors while smaller Sc atoms have extra space for movement. The difference in the atomic size (or ionic radius) of Y and Sc will inevitably cause the fluctuation of atoms from their perfect sites [50]. The resultant lattice distortion impedes dislocation movement, which enhances lattice strain and provides excess strength [51,52].

Table 1 A summary of the Vickers hardness (HV), fracture toughness (K_{IC}), biaxial flexural strength (δ_b), damage tolerance (D_t), and brittleness index (B) of the $(Y_{1-x}Sc_x)_2O_3$ ceramics

Sc content, x	HV (GPa)	K_{IC} (MPa·m$^{1/2}$)	δ_b (MPa)	D_t (m$^{1/2}$)	B (μm$^{-1/2}$)
0	6.71±0.01	1.16±0.12	81.48	0.379	5.78
0.091	8.04±0.14	1.27±0.07	94.22	0.300	6.33
0.167	8.42±0.17	1.39±0.09	96.38	0.307	6.06
0.231	9.44±0.10	1.56±0.11	106.64	0.277	6.05
0.286	9.69±0.14	1.40±0.08	111.76	0.231	6.92
0.310	9.62±0.16	1.21±0.14	120.86	0.186	7.95
0.355	9.55±0.01	1.11±0.06	92.39	0.225	8.60
0.412	9.45±0.14	1.32±0.17	92.54	0.270	7.16

The Vickers hardness (HV) and fracture toughness (K_{IC}) are important material parameters describing the resistance to deformation and crack propagation, and their ratio quantifies the brittleness index (B) [51,53], i.e.,

$$B = \frac{HV}{K_{IC}} \tag{6}$$

The brittleness index (B) can be used to quantitatively measure the machinability of ceramics. As shown in Table 1, the brittleness of the $(Y_{1-x}Sc_x)_2O_3$ solid solutions was higher than that of pristine Y_2O_3, which is related to the aggravated lattice distortion. As mentioned earlier, lattice distortion suppresses the movement of dislocations, makes deformation difficult, and makes ceramics more brittle.

On the other hand, neither brittleness nor fracture toughness (K_{IC}) alone can characterize the damage tolerance of a material. The damage tolerance is a property of a structure relating to its ability to sustain defects safely. According to the general definition proposed by Bao *et al.* [54], the damage tolerance (D_t) can be expressed as following:

$$D_t = \frac{K_{IC}}{\delta_b} \cdot \frac{E}{HV} \tag{7}$$

where K_{IC}/δ_b ratio indicates the degree of crack tolerance, while the E/HV item represents the capacity of energy dissipation. The calculated D_t values of the $(Y_{1-x}Sc_x)_2O_3$ ceramics are listed in Table 1. The formation of solid solution reduces the damage tolerance (D_t). For example, the values of damage tolerance were 0.379 and 0.231 $m^{1/2}$ for the samples with $x = 0$ and 0.286, respectively. The lower D_t values indicate that the solid solutions are more sensitive to defects and surface impact. Nevertheless, the damage tolerance of most $(Y_{1-x}Sc_x)_2O_3$ ceramics is still higher than that of SiC (0.113 $m^{1/2}$), ZrO_2 (0.194 $m^{1/2}$), and Al_2O_3 (0.255 $m^{1/2}$) [54]. The high hardness and fracture toughness (K_{IC}), as well as acceptable damage tolerance, indicate that the $(Y_{1-x}Sc_x)_2O_3$ transparent ceramics are capable of working in certain harsh environments.

4 Conclusions

In summary, using commercial Y_2O_3 and Sc_2O_3 powders as the starting materials, $(Y_{1-x}Sc_x)_2O_3$ transparent ceramics were successfully fabricated by the traditional solid state reaction in vacuum without any sintering additives. The experimental results show that Y_2O_3 and Sc_2O_3 can form a complete solid solution crystallizing in cubic bixbyite phase by high-temperature treatment. For the $(Y_{1-x}Sc_x)_2O_3$ solid solution series, with increasing Sc content (x), both the lattice constant and optical band-gap decrease. The decrease of lattice constant obeys the rule of mixtures, while the change in the band-gap deviates from the rule of mixtures, and the band-gap bowing is large and composition dependent.

The formation of $(Y_{1-x}Sc_x)_2O_3$ solid solution greatly reduces the melting point and effectively promotes the densification of the ceramics. The pristine Y_2O_3 ceramic is opaque, while the $(Y_{1-x}Sc_x)_2O_3$ solid solution ceramics become more and more transparent with the increase of Sc content (x), and achieve the highest transparency that almost equal to the theoretical transmittance of Y_2O_3 single crystal at $x = 0.286$. The $(Y_{0.714}Sc_{0.286})_2O_3$ sample exhibits a wide optically transparent wavelength range of 0.35–8 μm, and its in-line transmittance remains above 81% in the range of 0.6–6 μm, highlighting its advantages as laser host and window material. In terms of thermal performance, the thermal expansion coefficient (α) is almost independent of the composition, and the heat capacity (c_p) increases with the increase of Sc content (x), but due to the decrease of the photon mean free path, the thermal conductivity (k) of $(Y_{1-x}Sc_x)_2O_3$ ceramics still has a certain degree of decline. On the other hand, the mechanical properties including Vickers hardness (HV), fracture toughness (K_{IC}), and biaxial flexural strength (δ_b) are enhanced effectively due to the solid solution strengthening. However, the $(Y_{1-x}Sc_x)_2O_3$ solid solution ceramics exhibit smaller damage tolerance and higher brittleness compared with Y_2O_3, even though they also possess higher fracture toughness (K_{IC}), which requires further improvement in the future work.

Acknowledgements

This research was supported by Fujian Science & Technology Innovation Laboratory for Optoelectronic Information of China (2021ZZ113) and Strategic Priority Research Program of the Chinese Academy of Sciences (XDA22010301)

Electronic Supplementary Material

Supplementary material is available in the online version of this article at https://doi.org/10.1007/s40145-022-0584-4.

References

[1] Liu ZY, Ikesue A, Li J. Research progress and prospects of rare-earth doped sesquioxide laser ceramics. *J Eur Ceram Soc* 2021, **41**: 3895–3910.

[2] Zhang J, An LQ, Liu M, *et al*. Sintering of Yb^{3+}:Y_2O_3 transparent ceramics in hydrogen atmosphere. *J Eur Ceram Soc* 2009, **29**: 305–309.

[3] Jin LL, Zhou GH, Shimai S, *et al*. ZrO_2-doped Y_2O_3 transparent ceramics via slip casting and vacuum sintering. *J Eur Ceram Soc* 2010, **30**: 2139–2143.

[4] Fukabori A, Yanagida T, Pejchal J, *et al*. Optical and scintillation characteristics of Y_2O_3 transparent ceramic. *J Appl Phys* 2010, **107**: 073501.

[5] Zhang L, Yang J, Yu HY, *et al*. High performance of La-doped Y_2O_3 transparent ceramics. *J Adv Ceram* 2020, **9**: 493–502.

[6] Kränkel C, Uvarova A, Haurat É, *et al*. Czochralski growth of mixed cubic sesquioxide crystals in the ternary system Lu_2O_3–Sc_2O_3–Y_2O_3. *Acta Crystallogr Sect B* 2021, **77**: 550–558.

[7] Basyrova L, Loiko P, Jing W, *et al*. Spectroscopy and efficient laser operation around 2.8 μm of Er:$(Lu,Sc)_2O_3$ sesquioxide ceramics. *J Lumin* 2021, **240**: 118373.

[8] Xiao ZH, Yu SJ, Li YM, *et al*. Materials development and potential applications of transparent ceramics: A review. *Mater Sci Eng R Rep* 2020, **139**: 100518.

[9] Yavetskiy RP, Balabanov AE, Parkhomenko SV, *et al*. Effect of starting materials and sintering temperature on microstructure and optical properties of Y_2O_3:Yb^{3+} 5 at% transparent ceramics. *J Adv Ceram* 2020, **10**: 49–61.

[10] Pirri A, Maksimov RN, Shitov VA, *et al*. Continuously tuned $(Tm_{0.05}Sc_{0.252}Y_{0.698})_2O_3$ ceramic laser with emission peak at 2076 nm. *J Alloys Compd* 2021, **889**: 161585.

[11] Jing W, Loiko P, Basyrova L, *et al*. Spectroscopy and laser operation of highly-doped 10 at.% Yb:$(Lu,Sc)_2O_3$ ceramics. *Opt Mater* 2021, **117**: 111128.

[12] Liu LH, Morita K, Suzuki TS, *et al*. Synthesis of highly-infrared transparent Y_2O_3–MgO nanocomposites by colloidal technique and SPS. *Ceram Int* 2020, **46**: 13669–13676.

[13] Majima K, Niimi N, Watanabe M, *et al*. Effect of LiF addition on the preparation and transparency of vacuum hot pressed Y_2O_3. *Mater Trans JIM* 1994, **35**: 645–650.

[14] Yin DL, Wang J, Ni M, *et al*. Fabrication of highly transparent Y_2O_3 ceramics with CaO as sintering aid. *Materials* 2021, **14**: 444.

[15] Hou XR, Zhou SM, Li WJ, *et al*. Study on the effect and mechanism of zirconia on the sinterability of yttria transparent ceramic. *J Eur Ceram Soc* 2010, **30**: 3125–3129.

[16] Osipov VV, Orlov AN, Maksimov RN, *et al*. The influence of HfO_2 additives on the optical properties of Nd^{3+}-doped Y_2O_3 ceramics. *Phys Status Solidi C* 2013, **10**: 914–917.

[17] Li XK, Zhu QQ, Xu YY, *et al*. Optical and thermal properties of TiO_2-doped Y_2O_3 transparent ceramics synthesized by hot isostatic pressing. *J Am Ceram Soc* 2019, **102**: 2021–2028.

[18] Gan L, Park YJ, Zhu LL, *et al*. Fabrication and properties of La_2O_3-doped transparent yttria ceramics by hot-pressing sintering. *J Alloys Compd* 2017, **695**: 2142–2148.

[19] Osipov VV, Shitov VA, Maksimov RN, *et al*. Properties of transparent Re^{3+}:Y_2O_3 ceramics doped with tetravalent additives. *Opt Mater* 2015, **50**: 65–70.

[20] Xu XD, Hu ZW, Li DZ, *et al*. First laser oscillation of diode-pumped Tm^{3+}-doped $LuScO_3$ mixed sesquioxide ceramic. *Opt Express* 2017, **25**: 15322–15329.

[21] Pirri A, Toci G, Patrizi B, *et al*. Yb^{3+}:$(Lu_xY_{1-x})_2O_3$ mixed sesquioxide ceramics for laser applications. Part I: Fabrication, microstructure and spectroscopy. *J Alloys Compd* 2021, **869**: 159227.

[22] Chistyi IL, Fabelinskii IL, Kitaeva VF, *et al*. Experimental study of the properties of ZrO_2–Y_2O_3 and HfO_2–Y_2O_3 solid solutions. *J Raman Spectrosc* 1977, **6**: 183–192.

[23] Beil K, Saraceno CJ, Schriber C, *et al*. Yb-doped mixed sesquioxides for ultrashort pulse generation in the thin disk laser setup. *Appl Phys B* 2013, **113**: 13–18.

[24] Badie JM, Foex M. Determination experimentale, calcul et prevision de certains diagrammes Sc_2O_3–Ln_2O_3. *J Solid State Chem* 1978, **26**: 311–319. (in French)

[25] Badie JM. High-temperature phases and phase transitions in the systems Sc_2O_3–Ln_2O_3 (Ln = lanthanide and yttrium). *Rev Int Hautes Temp Refract* 1978, **15**: 183–199.

[26] Du PP, Huo D, Xi HQ, *et al*. Fabrication of nanocrystalline Sc_2O_3–Y_2O_3 solid solution ceramics by spark plasma sintering. *Ceram Int* 2017, **43**: 9854–9859.

[27] Zhang X, Gao S, Gui WH, *et al*. First-principles study of structure, mechanical and optical properties of La- and Sc-doped Y_2O_3. *J Rare Earths* 2019, **37**: 879–885.

[28] Pirri A, Patrizi B, Maksimov RN, *et al*. Spectroscopic investigation and laser behaviour of Yb-doped laser ceramics based on mixed crystalline structure $(Sc_xY_{1-x})_2O_3$. *Ceram Int* 2021, **47**: 29483–29489.

[29] Deng DQ, Xu L. Measurements of thermal expansion coefficient of phenolic foam at low temperatures. *Cryogenics* 2003, **43**: 465–468.

[30] Guguschev C, Hidde J, Gesing TM, *et al*. Czochralski growth and characterization of $Tb_xGd_{1-x}ScO_3$ and $Tb_xDy_{1-x}ScO_3$ solid-solution single crystals. *CrystEngComm* 2018, **20**: 2868–2876.

[31] Zhang L, Pan W. Structural and thermo-mechanical properties of Nd:Y_2O_3 transparent ceramics. *J Am Ceram Soc* 2015, **98**: 3326–3331.

[32] Yeheskel O, Tevet O. Elastic moduli of transparent yttria. *J Am Ceram Soc* 1999, **82**: 136–144.

[33] Shimizu Y, Ueda K. Phase formation and UV luminescence of Gd^{3+} doped perovskite-type $YScO_3$. *J Solid State Chem* 2016, **242**: 170–174.

[34] Li DZ, Liu J, Xu XD, *et al*. Spectral properties and laser operation of Nd^{3+}-doped mixed sesquioxide $LuYO_3$ ceramic. *J Lumin* 2021, **238**: 118282.

[35] Clark JB, Richter PW, Toit LD. High-pressure synthesis of $YScO_3$, $HoScO_3$, $ErScO_3$, and $TmScO_3$, and a reevaluation of the lattice constants of the rare earth scandates. *J Solid State Chem* 1978, **23**: 129–134.

[36] Giaquinta DM, zur Loye HC. Structural predictions in the ABO_3 phase diagram. *Chem Mater* 1994, **6**: 365–372.

[37] Uecker R, Velickov B, Klimm D, *et al*. Properties of rare-earth scandate single crystals (Re = Nd–Dy). *J Cryst Growth* 2008, **310**: 2649–2658.
[38] Jing W, Loiko P, Serres JM, *et al*. Synthesis, spectroscopy, and efficient laser operation of "mixed" sesquioxide Tm: $(Lu,Sc)_2O_3$ transparent ceramics. *Opt Mater Express* 2017, **7**: 4192–4202.
[39] Wei GC. Transparent ceramic lamp envelope materials. *J Phys D Appl Phys* 2005, **38**: 3057–3065.
[40] Tauc J, Grigorovici R, Vancu A. Optical properties and electronic structure of amorphous germanium. *Phys Status Solidi B* 1966, **15**: 627–637.
[41] He H, Cao YG, Fu RL, *et al*. Band gap energy and bowing parameter of In-rich InAlN films grown by magnetron sputtering. *Appl Surf Sci* 2010, **256**: 1812–1816.
[42] Koide Y, Itoh H, Khan MRH, *et al*. Energy band-gap bowing parameter in an $Al_xGa_{1-x}N$ alloy. *J Appl Phys* 1987, **61**: 4540–4543.
[43] Wei SH, Zunger A. Giant and composition-dependent optical bowing coefficient in GaAsN alloys. *Phys Rev Lett* 1996, **76**: 664–667.
[44] Moon CY, Wei SH, Zhu YZ, *et al*. Band-gap bowing coefficients in large size-mismatched II–VI alloys: First-principles calculations. *Phys Rev B* 2006, **74**: 233202.
[45] Shi HL, Duan Y. Band-gap bowing and p-type doping of (Zn,Mg,Be)O wide-gap semiconductor alloys: A first-principles study. *Eur Phys J B* 2008, **66**: 439–444.
[46] Nan CW. Physics of inhomogeneous inorganic materials. *Prog Mater Sci* 1993, **37**: 1–116.
[47] Bellaiche L, Wei S, Zunger A. Localization and percolation in semiconductor alloys: GaAsN vs GaAsP. *Phys Rev B Condens Matter* 1996, **54**: 17568–17576.
[48] Senkov ON, Scott JM, Senkova SV, *et al*. Microstructure and room temperature properties of a high-entropy TaNbHfZrTi alloy. *J Alloys Compd* 2011, **509**: 6043–6048.
[49] Gypen LA, Deruyttere A. Multi-component solid solution hardening. Part 1 proposed model *J Mater Sci* 1977, **12**: 1028–1033.
[50] Tsai MH, Yeh JW. High-entropy alloys: A critical review. *Mater Res Lett* 2014, **2**: 107–123.
[51] Xiang HM, Xing Y, Dai FZ, *et al*. High-entropy ceramics: Present status, challenges, and a look forward. *J Adv Ceram* 2021, **10**: 385–441.
[52] Boccaccini AR. Machinability and brittleness of glass-ceramics. *J Mater Process Technol* 1997, **65**: 302–304.
[53] Lawn BR, Marshall DB. Hardness, toughness, and brittleness: An indentation analysis. *J Am Ceram Soc* 1979, **62**: 347–350.
[54] Bao YW, Hu CF, Zhou YC. Damage tolerance of nanolayer grained ceramics and quantitative estimation. *Mater Sci Technol* 2006, **22**: 227–230.